ACS APPLIED ENERGY MATERIALS
Cite This: ACS Appl. Energy Mater. 2018, 1, 312−318
Letter
www.acsaem.org

Mutual Independence Ensured Long-Term Cycling Stability: Template-Free Electrodeposited Sn_4Ni_3 Nanoparticles as Anode Material for Lithium-Ion Batteries

Wenjun Deng,[†] Xusheng Wang,[‡] Chunyi Liu,[†] Chang Li,[†] Mianqi Xue,*[,†,‡] Rui Li,*[,†] and Feng Pan[†]

[†]School of Advanced Materials, Peking University Shenzhen Graduate School, Shenzhen 518055, China

[‡]Institute of Physics and Beijing National Laboratory for Condensed Matter Physics, Chinese Academy of Sciences, Beijing 100190, China

Supporting Information

ABSTRACT: The key challenge in utilizing tin-based intermetallic compounds for lithium-ion batteries (LIBs) is the poor cycling stability which is caused by the huge volume change during the alloying/de-alloying processes. In this work, concerning this issue, a novel template-free electrodeposition procedure to prepare mutual independent Sn_4Ni_3 nanoparticles is presented. As-fabricated Sn_4Ni_3 nanoparticles deliver a high reversible capacity of 388.9 mAh g^{-1} at a current density of 50 mA g^{-1}. Especially, such materials possess admirable cycling stability (no capacity fading after 1200 cycles at 200 mA g^{-1}) which can be attributed to the mutual independence of each nanoparticle. Combining with the high rate capability, the Sn_4Ni_3 nanoparticles present a promising future of long-life tin-based intermetallic LIB anodes.

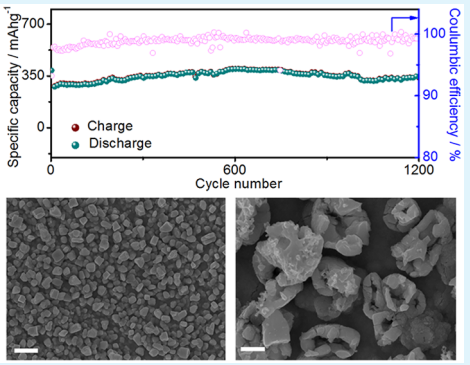

KEYWORDS: *Sn_4Ni_3 nanoparticles, long-term cycling stability, template-free electrodeposition, anode material, lithium-ion battery*

INTRODUCTION

Silicon- and tin-based materials are considered to be very appealing anodes of lithium-ion batteries (LIBs) owing to their intrinsic high specific capacity.[1] Systematic and admirable works (especially nanosilicon composites via Cui's group)[2,3] have been done, and great progress has been achieved in the field of silicon anode materials, leaving tin-based materials in need of more effort. The crux of poor cycling stability is one of the main obstacles to give full play of its high theoretical capacity ($Li_{4.4}Sn$, 994 mAh g^{-1}). And the key component in its poor cycling stability is the serious volume expansion and then pulverization during the alloying/de-alloying processes.

Strategies to improve the cycling stability always focus on the structure and space designs which are mainly based on the micro- and nanofabrication methods[4−11] with great advantages of reducing the path length of inward ion diffusion and enhancing the resistance to the structural pulverization.[12−14] A series of nanofabrication methods have been introduced in fabricating the tin-enriched or tin-based materials (such as $SnSe_2$,[15] SnSSe,[16,17] $MoS_{5.7}$,[18] Sn−Co,[19] and Sn−Ni alloys[20]) with nanometer sizes or micro-/nanostructures to improve the cycling stability. In general, template-assisted growth is a widely used method in fabricating tin-based nanomaterials.[21−23] Templates with specific structures, such as three-dimensional (3D) matrix substrate,[24−27] anodic aluminum oxide (AAO) template,[28] and polycarbonate porous template,[29] are frequently used to optimize the morphologies of the electrode materials. As early as 10 years ago, Hassoun et al. improved a Sn_4Ni_3 intermetallic nanostructured electrode via electrodeposition on a nanoarchitectured Cu substrate which could effectively accommodate the volume expansion during the cycling process, resulting in high rate capability with excellent capacity retention of 500 mAh g^{-1} with no decay after 200 cycles.[21] Recently, Tian and co-workers developed a simple way to build 3D Ni−Sn nanowire networks by using 3D porous AAO templates. Such 3D Ni−Sn nanowire networks can deliver a capacity as high as 4.3 mAh cm^{-2} with a cycle life over 50 cycles.[22]

However, despite the improved cycling stability in these works, the issue of long-term cycling stability still remains unsolved. Very recently, we reported a 3D core−shell Sn−Ni−Cu alloy@carbon nanorod which was fabricated by pulse electrodeposition with a polycarbonate porous template.[30] In our design, the novel nanoarchitecture can offer enough interspace for large volume expansion; thus the nanostructured electrodes exhibit almost 100% capacity retention over 400 cycles at 450 mA g^{-1}. Unfortunately, template-assisted methods are too expensive for commercialization. Moreover, the cycling stability of current Sn−Ni alloy electrodes, although superior to that of the pure Sn film electrode, is still not satisfactory enough for a longer cycling life. Herein, we report a novel template-free electrodeposition method to fabricate mutual independent Sn−

Received: December 9, 2017
Accepted: January 18, 2018
Published: January 18, 2018

DOI: 10.1021/acsaem.7b00242
ACS Appl. Energy Mater. 2018, 1, 312−318

Ni nanoparticles as LIB anode. A high reversible capacity of 388.9 mAh g^{-1} is demonstrated at a current density of 50 mA g^{-1}. Furthermore, long-life cycling stability is also achieved (no capacity fading after 1200 cycles at 200 mA g^{-1}), which should be assigned to the mutual independence of each nanoparticle. Together with the high rate capability, the Sn_4Ni_3 nanoparticles should be regarded as a promising candidate of tin-based anodes for long-life LIBs.

EXPERIMENTAL SECTION

Synthesis of the Sn_4Ni_3 Electrodes. The Sn_4Ni_3 electrodes were prepared by an electrodeposition method with a constant current at room temperature. A copper foil with 10 μm thickness was used as the cathode for the electrodeposition. Before depositing, the Cu foil was purified by dilute sulfuric acid (5 wt %) and then cleaned with ethanol and deionized water in turn. A rectangular plastic box was used for plating bath, and the size of the Cu foil used for electrodeposition is 4 × 5 cm^2. Electrodeposition processes were performed using a Maccor Series MC-16 battery testing system. All of the electrodes were electrodeposited for 20 min at a constant current density of 2 mA cm^{-2} with a Pt foil electrode as the anode. The components of the aqueous plating baths for depositing the Sn_4Ni_3 electrodes (named as electrode E1) and the compact $SnNi_{1.5}$ film (named as electrode E2) are given in Table 1. The solution for electrode E1 is pH 3 and the solution for electrode E2 is pH 8, which are adjusted by diluted sulfuric acid.

Table 1. Plating Bath Compositions for the Two Sn−Ni Alloy Electrodes

formulation	solution for E1 (mol L^{-1})	solution for E2 (mol L^{-1})
$SnSO_4$	0.01	0.01
$NiSO_4{\cdot}6H_2O$	0.01	0.01
potassium pyrophosphate ($K_4P_2O_7$)	0	0.1
sodium gluconate ($C_6H_{11}O_7Na$)	0.1	0
boric acid (H_3BO_3)	0.2	0
ammonium hydroxide (NH_4OH)	0	0.13
glycine (H_2NCH_2COOH)	0	0.05
Na_2SO_4	0.2	0.2

Material Characterizations. Crystal structures of the Sn−Ni alloys were measured by X-ray diffraction (XRD) with a Bruker generator working with Cu Kα radiation (λ = 1.5416 Å). Morphologies and chemical compositions of the Sn−Ni alloy electrodes were visualized by scanning electron microscopy (SEM; ZEISS SUPRA-55) equipped with an energy dispersive X-ray spectroscopy (EDX; Oxford X-Max) and X-ray photoelectron spectrometer (XPS; Thermo Scientific, Escalab 250Xi). The uniformity of the thin film surface was observed by a 3D laser confocal scanning microscope (VK-X200).

Electrochemical Tests of the Sn−Ni Alloy Electrodes. Electrochemical performances of the Sn−Ni alloy electrodes were characterized with lithium metal foils as the counter electrodes, Celgard 2400 as the separators, and 1 M lithium hexafluorophosphate ($LiPF_6$) in a mixture of ethylene carbonate (EC), dimethyl carbonate (DMC), and ethyl methyl carbonate (EMC) (v:v:v = 1:1:1) as the electrolyte, and then assembled into CR2032-type coin cells in an argon-filled glovebox. The average mass loading for both Sn−Ni alloy active materials on Cu substrates is about 0.4 mg cm^{-2}, which was measured by a microbalance (MS105 with a resolution of 0.01 mg). The cyclic voltammetry (CV) curves were carried out within the range of 0.01−2.0 V at a scanning rate of 0.1 mV s^{-1} using a CHI660C electrochemical system (Chenhua Instrument Co.). Electrochemical impedance spectroscopy (EIS) measurements were also performed on the CHI660D electrochemical system. All cells were galvanostatically charged and discharged at different current densities between 0.02 and 2.0 V by a battery cycler system (LAND-CT2001).

RESULT AND DISCUSSION

The Sn−Ni alloy electrodes were prepared by an electrodeposition method on the copper foils (with an average thickness of 10 μm) purified by dilute sulfuric acid with a constant current (2 mA cm^{-2}) for 20 min at room temperature with a Pt foil electrode as the anode. The components of aqueous plating baths for depositing the Sn_4Ni_3 electrodes (named as electrode E1) and the compact $SnNi_{1.5}$ film (named as electrode E2) are given in Table 1. The morphologies of electrodes E1 and E2 were evaluated by SEM (Figure 1a−d). Electrode E1 (Figure 1a,b) is composed of many nanoparticles with irregular shape and an average size of less than 400 nm. No exfoliation phenomenon occurs during the preparation process, indicating the integrated particle distribution, and this is favorable to reduce the length of the ion-diffusion path. As shown in Figure 1c,d, electrode E2 is accumulated with many closely packed nanoparticles. This configuration could not provide enough space to buffer the volume expansion and ensure sufficient electrolyte wettability inside the film during the lithiation process. The average thickness of the two thin film electrodes is 3−4 μm (as shown in Figure S1), and the surface roughness was observed through a 3D laser confocal scanning microscope. Three-dimensional scanning images show that E1 electrode has a higher integral flatness than E2 electrode (Figure S2). The morphologies and crystal structures of the two electrodes are reproducible in the different preparations (Figures S3−S5).

The crystal structures of the Sn−Ni alloys were measured by XRD with a Bruker generator working with Cu Kα radiation. The XRD patterns of electrodes E1 and E2 are separately shown in Figure 1e,f. The pattern of electrode E1 indicates a Sn_4Ni_3 crystalline phase (JCPDS No. 65-4310). The diffraction peak at 32.1° probably involves the presence of Sn as marked in Figure 1e. As for the pattern of electrode E2, a $SnNi_{1.5}$ alloy phase with hexagonal structure (space group, $p6_3/mmc$) is detected with two main 2θ peaks at 30.6 and 44.2° corresponding to crystal planes of (101) and (110), respectively, which could be attributed to a reference $SnNi_{1.5}$ intermetallic compound (JCPDS No. 65-9460).

The surface elemental composition of electrodes E1 and E2 were determined by EDX (Figure 2a,b, respectively) and XPS (Figure 2c,d, respectively), respectively. Quantitative information was also provided by EDX (as shown in Figure S6a,b, respectively), the atomic ratios of Sn:Ni are 29.2:23.7 for electrode E1 and 27.2:29.7 for electrode E2, respectively. Both of the electrodes reveal the homogeneous distributions of Cu, Sn, and Ni elements, suggesting that both the Sn_4Ni_3 and $SnNi_{1.5}$ species are evenly distributed across the surfaces of the Cu foils. The atomic ratio of Ni to Sn in the electrode E1 is lower than that of electrode E2 owing to a different electrochemical reactivity of Ni in the two plating baths (it is easier to deposit Ni under an alkaline condition than an acidic condition at room temperature). XPS spectra confirm the

DOI: 10.1021/acsaem.7b00242
ACS Appl. Energy Mater. 2018, 1, 312−318

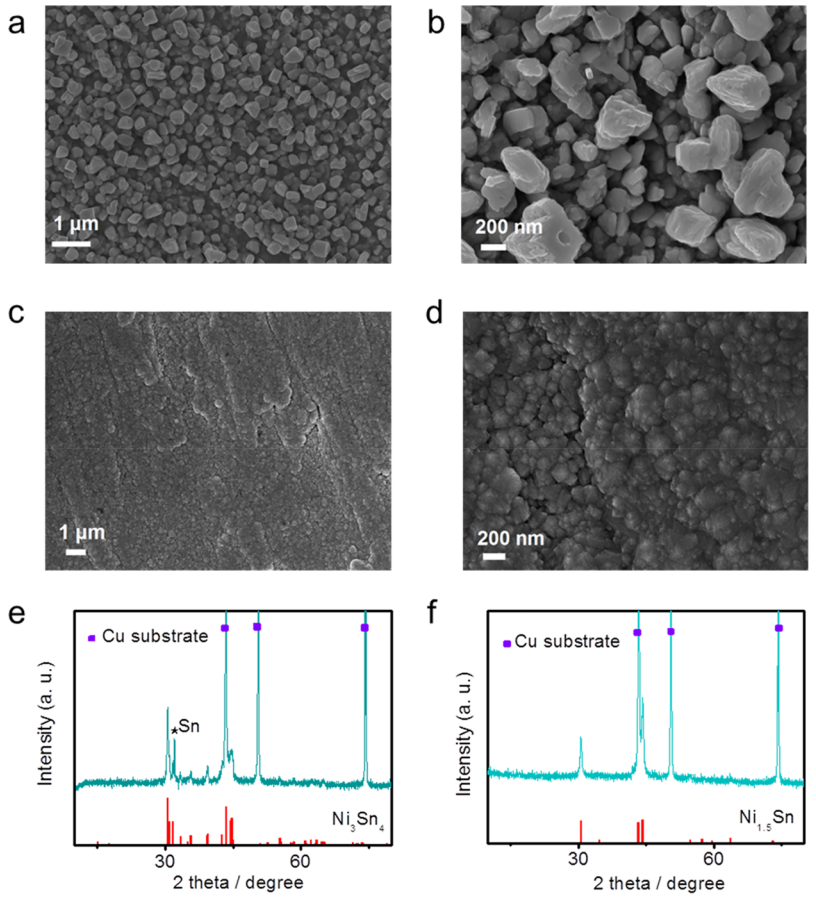

Figure 1. Characterizations of the E1 and E2 electrodes. (a, b) SEM images of the electrode E1. (c, d) SEM images of the electrode E2. XRD patterns of the electrodes E1 (e) and E2 (f).

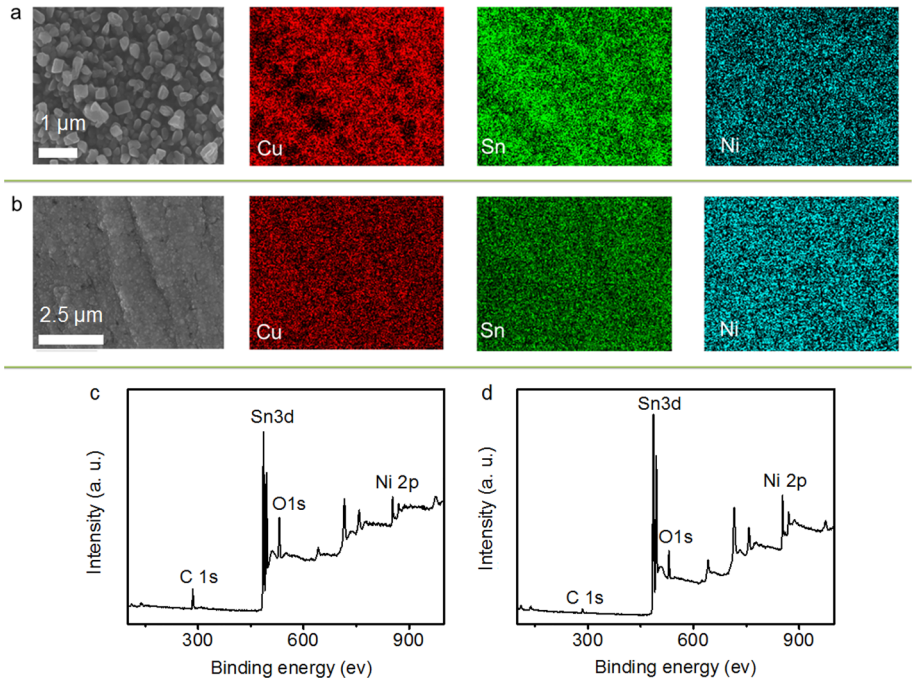

Figure 2. EDX images of the electrode E1 (a) and E2 (b). Both of the electrodes demonstrate the homogeneous distribution of Cu, Sn, and Ni elements. XPS spectra of the electrode E1 (c) and E2 (d), respectively.

existence of Sn and Ni elements on the surfaces of both electrodes. Also, notice that strong O 1s XPS signals (530 ev) are observed in both spectra, but they disappear after Ar^+ sputtering 300 s (Figure S7a,b, respectively). This indicates that

DOI: 10.1021/acsaem.7b00242
ACS Appl. Energy Mater. 2018, 1, 312−318

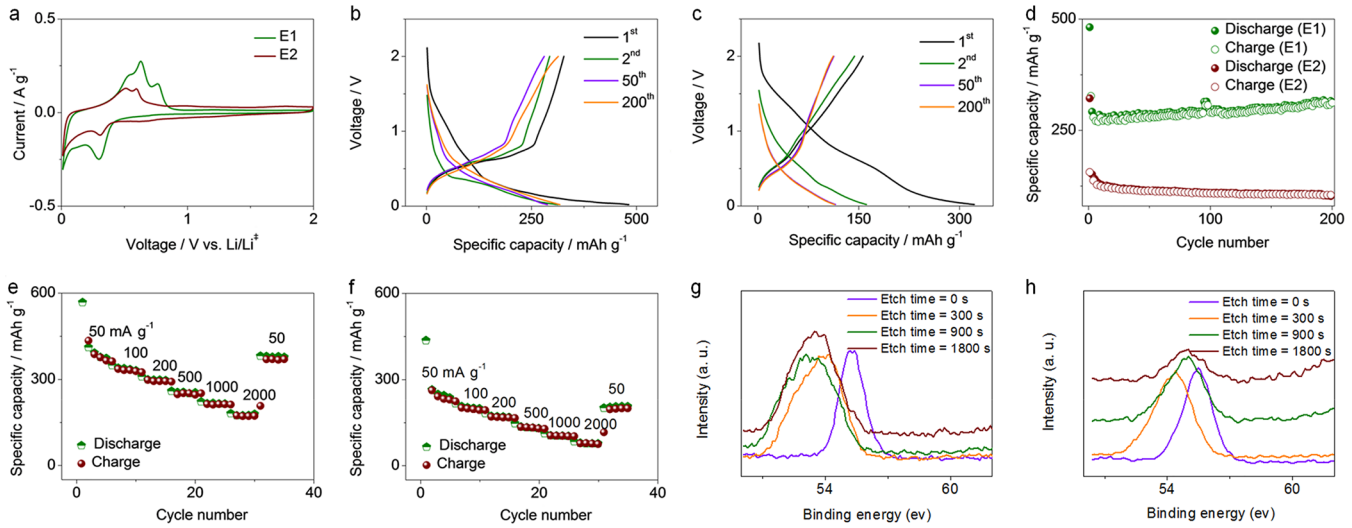

Figure 3. Electrochemical performances of the electrodes E1 and E2. (a) Typical cyclic voltammogram (CV) curves of electrodes E1 and E2 (both third cycle) performed between 0.01 and 2.0 V at a scan rate of 0.1 mV s^{-1}. Discharge−charge curves of the electrode E1 (b) and E2 (c) at a current density of 200 mA g^{-1}. (d) Cycling performances of the two electrodes at 200 mA g^{-1}. Rate capability of the electrode E1 (e) and E2 (f). Li 1s spectra of the fully discharged electrodes E1 (g) and E2 (h) after 10 cycles.

the metallic elements on the surface were oxidized. Sn 3d and Ni 2p spectra before and after Ar^+ sputtering demonstrate the presence of high-valence Sn only on the surface (not in the bulk) of electrode E1 (Figure S7c) and no change for Ni (Figure S7d).

Figure 3a exhibits the CV curves of electrodes E1 and E2 within the voltage range of 0.01−2.0 V at 0.1 mV s^{-1}. During the cathodic scan process, the reduction peaks located at 0.30 and 0.31 V (electrodes E1 and E2, respectively) should be assigned to the process of lithium-ion insertion into Sn_4Ni_3 and $SnNi_{1.5}$ species. And the following reduction peaks located at 0.01 V for both the electrodes could be assigned to the alloying reaction with $Li_{4.4}Sn$ as the product. During the following anodic scan process, the de-alloying reaction occurs for both of the electrodes (0.63 and 0.51 V for the electrodes E1 and E2, respectively). Then the oxidation peaks located at 0.76 and 0.60 V should separately correspond to the extraction process of lithium ions from the Sn_4Ni_3 and $SnNi_{1.5}$ species. The lithiation/delithiation mechanisms can be described as the following reactions:[31]

$$NiSn_x + 4.4xLi^+ \rightarrow xLi_{4.4}Sn + Ni \quad \text{(lithiation)} \qquad (1)$$

$$Li_{4.4}Sn \leftrightarrow Sn + 4.4Li^+ + 4.4e^- \quad \text{(delithiation)} \qquad (2)$$

The galvanostatic voltage profiles of electrodes E1 and E2 are demonstrated for several cycles in Figure 3b,c. The first discharge capacity of electrode E1 is as high as 481.5 mAh g^{-1}, and the Coulombic efficiency is 67.9% (subsequent efficiency data see Figure S8). Both two values are much higher than that of 321.7 mAh g^{-1} and 48.6% for electrode E2. This should be caused by the poor electrolyte wettability inside the closely packed $SnNi_{1.5}$ nanoparticles. In addition, according to the rule of reversed stability,[32,33] a higher alloy formation enthalpy makes the alloy more stable. Considering the formation enthalpy of $SnNi_{1.5}$ is higher than that of Sn_4Ni_3, it can be concluded that the higher stability of $SnNi_{1.5}$ could increase the difficulty of lithium-ion insertion and thus decrease the theoretical capacity.[34] The initial irreversible capacity for both of the electrodes should be attributed to the formation of the solid electrolyte interphase (SEI) film and the irreversible alloy phase during lithium intercalation.[35,36] The surface elements of electrode E1 after 10 cycles were analyzed by XPS (Figure S9), which shows obvious C, O, and F 1s signals but hardly appreciable Ni and Sn signals, indicating the existence of a relatively thick SEI film. The following second, 50th, and 200th cycles of electrode E1 also show much higher capacity deliveries than those of electrode E2.

Cycling performances of the two electrodes are shown in Figure 3d; it can be found that the cycling stability of electrode E1 is much better than that of electrode E2 at 200 mA g^{-1}. Electrode E1 exhibits a high discharge capacity of 317.3 mAh g^{-1} without fading after 200 cycles, which is only 103.2 mAh g^{-1} for electrode E2 after 200 cycles with serious capacity fading. Electrode E1 (Figure 3e) also shows much better rate capability than that of electrode E2 (Figure 3f). The average discharge capacities are 388.9, 338.6, 300.6, 255.2, 217.5, and 179.4 mAh g^{-1} for electrode E1 at the current densities of 50, 100, 200, 500, 1000, and 2000 mA g^{-1}, respectively. And the capacity could recover to 381.0 mAh g^{-1} when the current density is back to 50 mA g^{-1}. In contrast, electrode E2 could only keep 30.5% retention of the initial capacity at the current density of 2000 mA g^{-1}. The excellent rate capability of electrode E1 is a result of fast lithium-ion transport due to the mutual independence of each Sn_4Ni_3 nanoparticle (Figure S10). To find out the reason for the significant difference in electrochemical performance of the two electrodes, surface-sensitive technique XPS was conducted on fully discharged Sn−Ni electrodes with various Ar^+ sputtering. For electrode E1, Li 1s spectra in Figure 3g exhibit a strong signal and peak area without any decrease even when the etch time reaches 1800 s, while the peak area decreases dramatically after etching 1800 s (as shown in Figure 3h). Compared to that of the $SnNi_{1.5}$ electrode, the fully discharged Sn_4Ni_3 electrode demonstrates superior vertical reaction dimension during the lithiation process, which has been confirmed by the above results of time-controlled Ar^+ sputtering XPS characterizations. This indicates the good electrolyte wettability in the Sn_4Ni_3 electrode. And enough interspace among the Sn_4Ni_3 nanoparticles can effectively accommodate the volume expansion, then allowing high capacity delivery and cycling stability.

DOI: 10.1021/acsaem.7b00242
ACS Appl. Energy Mater. 2018, 1, 312−318

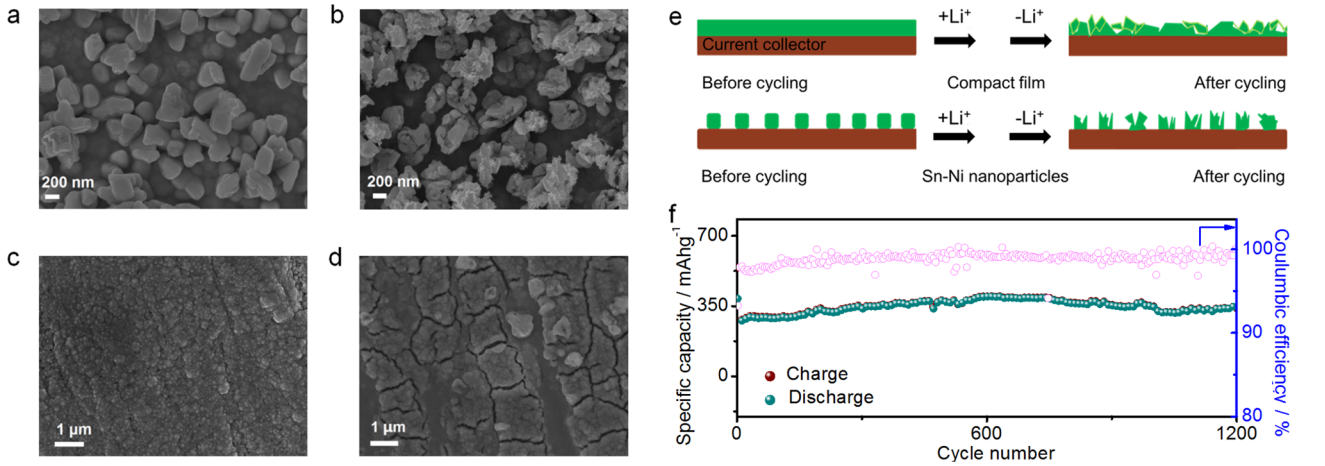

Figure 4. SEM images of the electrode E1 (Sn_4Ni_3 nanoparticles), pristine electrode (a) and after 100 cycles (b). SEM images of the electrode E2 ($SnNi_{1.5}$ film), pristine electrode (c) and after 100 cycles (d). (e) Schematics of the electrodes E1 and E2 before and after cycling. (f) Long-term cycling performance of the electrode E1 at 200 mA g^{-1}.

Morphology changes of both the cycled electrodes have been characterized. Panels a and b of Figure 4 show the SEM images of electrode E1 before and after 100 cycles. As compared to Figure 1a,b, the flowering expanded nanostructured Sn_4Ni_3 nanoparticles can be clearly observed compared to the pristine nanoparticles; nearly a 2 times change in size is induced due to the Li^+ insertion during the discharge process. Remarkably, due to enough interspace among the nanoparticles, the Sn_4Ni_3 species do not drop off from the current collector despite the volume expansion, and the small cracks are generated to form a porous structure which could increase the active sites of Sn_4Ni_3 nanoparticles, thus allowing the increased capacity delivery of electrode E1. More importantly, the pulverization phenomenon of Sn_4Ni_3 nanoparticles usually generated from a huge volume change is not observed in this work due to the effective buffer effect of the large free space among the nanoparticles.[9] As a consequence, electrode E1 exhibits superior cycling stability. Panels c and d of Figure 4 display the morphology change of electrode E2 before and after 100 cycles. As compared to Figure 1c,d, the phenomena of pulverization and exfoliation are also not observed in the $SnNi_{1.5}$ film while the cycling process induces some cracks on the surface with the average thickness of less than 0.2 μm and length of less than 1 μm. Yet the issue of poor electrolyte wettability inside the closely packed $SnNi_{1.5}$ nanoparticles still limits the capacity delivery and cycling stability of electrode E2. The structural changes of both electrodes have also been analyzed through XRD (Figure S11). It can be observed that the lithiation process has the effect of lowering the crystallinity of the electrodes, and no more formation of new phases can be confirmed compared with the pristine electrodes. The reaction mechanism of Sn−Ni alloys can be suggested as follows: Sn species segregates from Sn−Ni alloy and with Li to form the Li−Sn alloy during the intercalation of lithium into Sn−Ni alloy at the discharge process, and with the extraction of lithium from the Li−Sn alloy during the charge process, the de-alloyed Sn species recombines with the Ni atom again to form the Sn−Ni alloy phase to keep the original structure. Schematics of the electrodes E1 and E2 before and after cycling are illustrated in Figure 4e. Small cracks can be observed on the surface of both electrodes E1 and E2. There is plenty of interspace for the Sn_4Ni_3 nanoparticles to accommodate the volume expansion and realize high electrolyte wettability. Yet these strengths could not be achieved in electrode E2, thus leading to the continuous capacity loss. As shown in Figure 4f, the long-term cycling stability of electrode E1 is also assessed at 200 mA g^{-1}. After 1200 cycles, electrode E1 still delivers a reversible capacity of 330.0 mAh g^{-1} with no capacity fading (compared with the second cycle as shown in Figure S12). The superior cycling stability has not been reported previously among the Sn−Ni alloy electrodes.[20,25,37−41]

CONCLUSION

In conclusion, we developed a facile template-free electrodeposition method to build the mutual independent Sn_4Ni_3 nanoparticles as LIB anodes. A high reversible capacity of 388.9 mAh g^{-1} is demonstrated at a current density of 50 mA g^{-1} for the Sn_4Ni_3 electrodes. And long-term cycling stability is realized, documented by the high capacity retention of 330.0 mAh g^{-1} (no capacity fading) after 1200 cycles at 200 mA g^{-1}. The high performance could be assigned to the mutual independence of each nanoparticle, which is favorable to buffer the volume expansion and improve the electrolyte wettability. The Sn_4Ni_3 electrodes also achieve high rate capability. Thus, the Sn_4Ni_3 nanoparticles provide a bright future of long-lived tin-based LIB anodes.

ASSOCIATED CONTENT

Supporting Information

The Supporting Information is available free of charge on the ACS Publications website at DOI: 10.1021/acsaem.7b00242.

Additional information on the experimental descriptions (PDF)

AUTHOR INFORMATION

Corresponding Authors

*(R.L.): E-mail: lirui@pkusz.edu.cn.
*(M.X.): E-mail: xuemq@iphy.ac.cn.

ORCID

Mianqi Xue: 0000-0002-6023-2618
Rui Li: 0000-0001-5480-8089
Feng Pan: 0000-0002-8216-1339

Notes

The authors declare no competing financial interest.

DOI: 10.1021/acsaem.7b00242
ACS Appl. Energy Mater. 2018, 1, 312−318

■ ACKNOWLEDGMENTS

We thank Dr. X. Ma for support of this project. This work was supported by the Shenzhen Science and Technology Research Grant (JCYJ20160531141109132 and JCYJ20170412150450297), the National Natural Science Foundation of China (Grants 21622407 and 21404009), and Guangdong Innovative and Entrepreneurial Research Team Progress (Grant 2013N080).

■ REFERENCES

(1) Scrosati, B.; Hassoun, J.; Sun, Y. K. Lithium-ion batteries. A look into the future. *Energy Environ. Sci.* **2011**, *4*, 3287−3295.
(2) Cui, L.-F.; Yang, Y.; Hsu, C. M.; Cui, Y. Carbon-Silicon Core-Shell Nanowires as High Capacity Electrode for Lithium Ion Batteries. *Nano Lett.* **2009**, *9*, 3370−3374.
(3) Choi, S.; Kwon, T. W.; Coskun, A.; Choi, J. W. Highly elastic binders integrating polyrotaxanes for silicon microparticle anodes in lithium ion batteries. *Science* **2017**, *357*, 279−283.
(4) Taberna, L.; Mitra, S.; Poizot, P.; Simon, P.; Tarascon, J. M. High rate capabilities Fe3O4-based Cu nano-architectured electrodes for lithium-ion battery applications. *Nat. Mater.* **2006**, *5*, 567−573.
(5) Xue, M.; Chen, D.; Long, Y.; Wang, P.; Zhao, L.; Chen, G. Direct Pen Writing of High-T_c Flexible Magnesium Diboride Superconducting Arrays. *Adv. Mater.* **2015**, *27*, 3614−3619.
(6) Xue, M.; Li, F.; Cao, T. Fabrication of ultra-fine nanostructures using edge transfer printing. *Nanoscale* **2012**, *4*, 1939−1947.
(7) Ma, X.; Xue, M.; Li, F.; Chen, J.; Chen, D.; Wang, X.; Pan, F.; Chen, G. F. Gradual-order enhanced stability: a frozen section of electrospun nanofibers for energy storage. *Nanoscale* **2015**, *7*, 8715−8719.
(8) Xue, M.; Chen, D.; Wang, X.; Chen, J.; Chen, G. F. Carbonized poly(vinylidene fluoride)/graphene oxide with three-dimensional multiscale-pore architecture as an advanced electrode material. *J. Mater. Chem. A* **2015**, *3*, 7715−7718.
(9) Wang, H.; Yang, Y.; Liang, Y.; Robinson, J. T.; Li, Y.; Jackson, A.; Cui, Y.; Dai, H. Graphene-Wrapped Sulfur Particles as a Rechargeable Lithium-Sulfur Battery Cathode Material with High Capacity and Cycling Stability. *Nano Lett.* **2011**, *11*, 2644−2647.
(10) Simon, P.; Gogotsi, Y. Materials for electrochemical capacitors. *Nat. Mater.* **2008**, *7*, 845−854.
(11) Xue, M.; Ma, X.; Xie, Z.; Duan, L.; Jiang, Y.; Zhang, M.; Cao, T. Fabrication of Gold−Directed Conducting Polymer Nanoarrays for High−Performance Gas Sensor. *Chem. - Asian J.* **2010**, *5*, 2266−2270.
(12) Bruce, P. G.; Scrosati, B.; Tarascon, J. M. Nanomaterials for rechargeable lithium batteries. *Angew. Chem., Int. Ed.* **2008**, *47*, 2930−2946.
(13) Liu, C.; Li, F.; Ma, L. P.; Cheng, H. M. Advanced Materials for Energy Storage. *Adv. Mater.* **2010**, *22*, E28−E62.
(14) Guo, Y. G.; Hu, J. S.; Wan, L. J. Nanostructured materials for electrochemical energy conversion and storage devices. *Adv. Mater.* **2008**, *20*, 2878−2887.
(15) Wang, X.; Yang, Z.; Wang, C.; Chen, D.; Li, R.; Zhang, X.; Chen, J.; Xue, M. Buffer layer enhanced stability of sodium-ion storage. *J. Power Sources* **2017**, *369*, 138−145.
(16) Yang, Z.; Liang, H.; Wang, X.; Ma, X.; Zhang, T.; Yang, Y.; Xie, L.; Chen, D.; Long, Y.; Chen, J.; Chang, Y.; Yan, C.; Zhang, X.; Zhang, X.; Ge, B.; Ren, Z.; Xue, M.; Chen, G. Atom-Thin SnS2-xSex with Adjustable Compositions by Direct Liquid Exfoliation from Single Crystals. *ACS Nano* **2016**, *10*, 755−762.
(17) Wang, X.; Chen, D.; Yang, Z.; Zhang, X.; Wang, C.; Chen, J.; Zhang, X.; Xue, M. Novel Metal Chalcogenide SnSSe as a High-Capacity Anode for Sodium-Ion Batteries. *Adv. Mater.* **2016**, *28*, 8645−8650.
(18) Wang, X.; Du, K.; Wang, C.; Ma, L.; Zhao, B.; Yang, J.; Li, M.; Zhang, X.-X.; Xue, M.; Chen, J. Unique Reversible Conversion-Type Mechanism Enhanced Cathode Performance in Amorphous Molybdenum Polysulfide. *ACS Appl. Mater. Interfaces* **2017**, *9*, 38606−38611.
(19) Tamura, N.; Fujimoto, A.; Kamino, M.; Fujitani, S. Mechanical stability of Sn-Co alloy anodes for lithium secondary batteries. *Electrochim. Acta* **2004**, *49*, 1949−1956.
(20) Mukaibo, H.; Sumi, T.; Yokoshima, T.; Momma, T.; Osaka, T. Electrodeposited Sn-Ni alloy film as a high capacity anode material for lithium-ion secondary batteries. *Electrochem. Solid-State Lett.* **2003**, *6*, A218−A220.
(21) Hassoun, J.; Panero, S.; Simon, P.; Taberna, P. L.; Scrosati, B. High-rate, long-life Ni-Sn nanostructured electrodes for lithium-ion batteries. *Adv. Mater.* **2007**, *19*, 1632−1635.
(22) Tian, M.; Wang, W.; Wei, Y.; Yang, R. Stable high areal capacity lithium-ion battery anodes based on three-dimensional Ni-Sn nanowire networks. *J. Power Sources* **2012**, *211*, 46−51.
(23) Deng, D.; Kim, M. G.; Lee, J. Y.; Cho, J. Green energy storage materials: Nanostructured TiO2 and Sn-based anodes for lithium-ion batteries. *Energy Environ. Sci.* **2009**, *2*, 818−837.
(24) Xue, M.; Wang, Y.; Wang, X.; Huang, X.; Ji, J. Single−Crystal−Conjugated Polymers with Extremely High Electron Sensitivity through Template−Assisted In Situ Polymerization. *Adv. Mater.* **2015**, *27*, 5923−5929.
(25) Huang, L.; Wei, H. B.; Ke, F. S.; Fan, X. Y.; Li, J. T.; Sun, S. G. Electrodeposition and lithium storage performance of three-dimensional porous reticular Sn-Ni alloy electrodes. *Electrochim. Acta* **2009**, *54*, 2693−2698.
(26) Shin, H. C.; Liu, M. L. Three-dimensional porous copper-tin alloy electrodes for rechargeable lithium batteries. *Adv. Funct. Mater.* **2005**, *15*, 582−586.
(27) Zhu, J.; Xue, M.; Zhao, D.; Zhang, M.; Duan, L.; Qiu, Y.; Cao, T. Facile Fabrication of Metallic Nanostructures by Tunable Cracking and Transfer Printing. *Angew. Chem., Int. Ed.* **2011**, *50*, 12478−12482.
(28) Xue, M.; Li, F.; Chen, D.; Yang, Z.; Wang, X.; Ji, J. High-Oriented Polypyrrole Nanotubes for Next-Generation Gas Sensor. *Adv. Mater.* **2016**, *28*, 8265−8270.
(29) Ferrara, G.; Damen, L.; Arbizzani, C.; Inguanta, R.; Piazza, S.; Sunseri, C.; Mastragostino, M. SnCo nanowire array as negative electrode for lithium-ion batteries. *J. Power Sources* **2011**, *196*, 1469−1473.
(30) Peng, H.; Li, R.; Hu, J.; Deng, W.; Pan, F. Core-Shell Sn-Ni-Cu-Alloy@Carbon Nanorods to Array as Three-Dimensional Anode by Nanoelectrodeposition for High-Performance Lithium Ion Batteries. *ACS Appl. Mater. Interfaces* **2016**, *8*, 12221−12227.
(31) Hassoun, J.; Panero, S.; Scrosati, B. Electrodeposited Ni−Sn intermetallic electrodes for advanced lithium ion batteries. *J. Power Sources* **2006**, *160*, 1336−1341.
(32) Vanmal, H. H.; Buschow, K. H. J.; Miedema, A. R. Hydrogen absorption in LaNiâ and related compounds: experimental observations and their explanation. *J. Less-Common Met.* **1974**, *35*, 65−76.
(33) Chen, D.; Wang, X.; Chen, J.; Ren, Z.; Xue, M.; Chen, G. Rewriting the Superconductivity in Iron-Based Superconductors by Lithium-Ion Insertion and Extraction. *Adv. Mater.* **2015**, *27*, 4224−4228.
(34) Qin, H.; Zhao, X.; Jiang, N.; Li, Z. Solvothermal synthesis and ex situ XRD study of nano-Ni3Sn2 used as an anode material for lithium-ion batteries. *J. Power Sources* **2007**, *171*, 948−952.
(35) Wang, G.; Wang, B.; Wang, X.; Park, J.; Dou, S.; Ahn, H.; Kim, K. Sn/graphene nanocomposite with 3D architecture for enhanced reversible lithium storage in lithium ion batteries. *J. Mater. Chem.* **2009**, *19*, 8378−8384.
(36) Zhu, X. J.; Guo, Z. P.; Zhang, P.; Du, G. D.; Poh, C. K.; Chen, Z. X.; Li, S.; Liu, H. K. Three-dimensional reticular tin-manganese oxide composite anode materials for lithium ion batteries. *Electrochim. Acta* **2010**, *55*, 4982−4986.
(37) Yamamoto, T.; Nohira, T.; Hagiwara, R.; Fukunaga, A.; Sakai, S.; Nitta, K. Charge-discharge behavior of Sn-Ni alloy film electrodes in an intermediate temperature ionic liquid for the electrolyte of a sodium secondary battery. *Electrochim. Acta* **2016**, *193*, 275−283.
(38) Jiang, D.; Ma, X.; Fu, Y. High-performance Sn-Ni alloy nanorod electrodes prepared by electrodeposition for lithium ion rechargeable batteries. *J. Appl. Electrochem.* **2012**, *42*, 555−559.

DOI: 10.1021/acsaem.7b00242
ACS Appl. Energy Mater. 2018, 1, 312−318

(39) Zhuo, K.; Jeong, M. G.; Chung, C. H. Highly porous dendritic Ni-Sn anodes for lithium-ion batteries. *J. Power Sources* **2013**, *244*, 601−605.
(40) Polat, B. D.; Abouimrane, A.; Sezgin, N.; Keles, O.; Amine, K. Use of Multilayered Ni-Sn and Ni-Sn-C Thin Film Anodes for Lithium-Ion Batteries. *Electrochim. Acta* **2014**, *135*, 585−593.
(41) Sengupta, S.; Patra, A.; Akhtar, M.; Das, K.; Majumder, S. B.; Das, S. 3D microporous Sn-Sb-Ni alloy impregnated Ni foam as high-performance negative electrode for lithium-ion batteries. *J. Alloys Compd.* **2017**, *705*, 290−300.

DOI: 10.1021/acsaem.7b00242
ACS Appl. Energy Mater. 2018, 1, 312−318